Copyright

by

Anthony Vincent Oliveri

2014

The Thesis committee for Anthony Vincent Oliveri

Certifies that this is the approved version of the following thesis:

The Impact of X-rays on Primordial Minihalos

APPROVED BY

SUPERVISING COMMITTEE:

Supervisor: _____

Volker Bromm

_____

Don Winget

The Impact of X-rays on Primordial Minihalos

by

Anthony Vincent Oliveri

Thesis

Presented in Partial Fulfillment

of the Requirements

for the Degree of

Bachelor of Science in Astronomy

The University of Texas at Austin

May 2014

Acknowledgments

I would like to thank my advisor, Dr. Volker Bromm, for guiding me through the entirety of my research project. His extensive knowledge, patience, and advice have been invaluable to me. I also owe much of the success of my project to UT's former graduate student Athena Stacy, who provided me with the code used in the minihalo simulations, as well as to Jacob Hummel and Myoungwon Jeon, who helped me through parts of my project that I got stuck on. Finally, I am tremendously grateful to my parents, whose unwavering support has made all of this possible.

Anthony Vincent Oliveri

The University of Texas at Austin

May 2014

The Impact of X-rays on Primordial Minihalos

by

Anthony Vincent Oliveri, B.S.
The University of Texas at Austin, 2014
SUPERVISOR: Volker Bromm

One of the current problems in cosmology is to understand how the first gravitationally-bound objects, or dark matter minihalos, evolved to form chemically rich, star-forming galaxies. The first stars to exist are believed to have formed in the center of minihalos that have cooled and collapsed enough to fragment into stellar-sized gas clouds. However, to reach such low temperatures, minihalos needed a more effective coolant than atomic hydrogen, namely molecular hydrogen (H_2). The formation of H_2 could be catalyzed by an x-ray background, which is expected to originate primarily from high-mass x-ray binaries (HMXBs). By simulating the collapse of a minihalo in the presence of x-ray backgrounds of varying strengths, we ascertain the resulting properties of a minihalo and compare to the case of no x-ray background. For sufficiently weak backgrounds (energy density $u_{\rm XR} < 10^{-16}{\rm J/m^3}$), a minihalo can cool to lower temperatures than without an x-ray background, leading to the formation of lower mass stars. The mass of these primitive stars affected the abundance of heavy chemical elements that formed during their deaths as supernovae, which in turn influenced how the earliest galaxies formed.

Contents

Acknowledgments **iv**

Abstract **v**

Chapter 1 Introduction: History of the Early Universe **1**

Chapter 2 Methods **9**

Chapter 3 Results **18**

Chapter 4 Conclusion **26**

Bibliography **29**

Chapter 1

Introduction: History of the Early Universe

1.1 The Cosmic Dark Ages

Shortly after its birth in the Big Bang, our universe was relatively simple in structure. It was composed of a homogeneous mixture of electromagnetic radiation, ordinary matter (protons, electrons, and neutrons) in ionized form, neutrinos, and dark matter. One of the primary goals of cosmologists is to understand how the universe evolved from this simple state to the complex, galaxy-filled universe of the present, 14 billion years later. In this introduction, I succinctly summarize the comprehensive exposition given in Loeb (2010).

Since its inception in the Big Bang, the universe has been continually expanding and cooling. Roughly 400,000 years after the Big Bang, the matter in the universe had cooled enough for protons and electrons to undergo recombination, allowing ordinary matter to

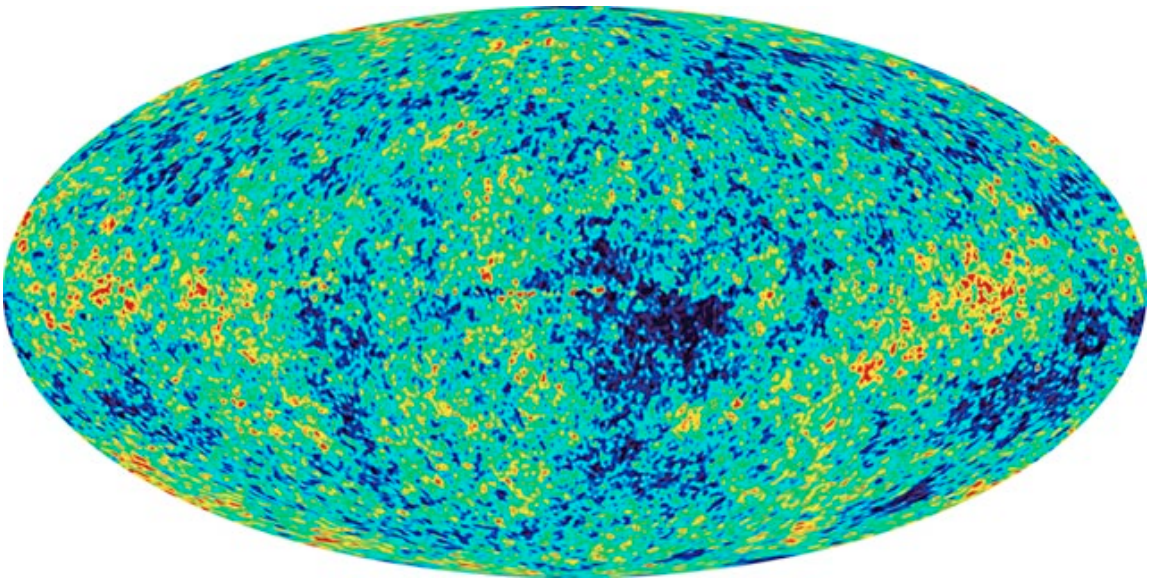

Figure 1.1 The high-resolution map of the CMB taken by the Wilkinson Microwave Anisotropy Probe that illustrates the density perturbations 380,000 years after the Big Bang. Regions that are towards the red end of the spectrum have a higher temperature (corresponding to higher gas densities) and regions towards the blue end have lower temperatures (corresponding to lower gas densities). The density fluctuations are on the order of one part in $\sim 10^5$. Credit NASA/WMAP science team (http://map.gsfc.nasa.gov/).

transition from plasma to neutral gas (primarily hydrogen and helium, with trace amounts of lithium). With the plasma no longer coupled to radiation, the photons became free to travel throughout the universe with little scattering. The resulting temperature distribution in the Cosmic Microwave Background (CMB) radiation has been measured to a high degree of accuracy by the Wilkinson Microwave Anisotropy Probe (WMAP), pictured in Figure 1.1.

As photons continued to be redshifted by cosmic expansion into wavelengths beyond the visible regime, the universe entered the cosmological dark ages. Since no stars had yet

formed, the dark ages were devoid of any visible sources of light. Cosmologists advance their models of the universe by performing computational simulations to predict how the universe evolved given the initial conditions seen in the CMB. My thesis is part of the effort to use numerical simulations to predict how the matter in the universe collapsed to form the first stars and, later, the first galaxies.

1.2 Cosmological Structure Formation

The temperature perturbations seen in the CMB radiation (Fig. 1.1) correspond to fluctuations in the matter density; those fluctuations are vital to future structure formation. Without the existence of these perturbations, the expansion of the universe would have prevented the primordial gas to collapse to form stars and galaxies, causing the Dark Ages to perpetuate indefinitely. Indeed, this could have been the case, since the diffusion of photons in the early universe would have smoothed any density enhancements in the gas. However, the perturbations that formed in the very early universe were preserved by dark matter, which comprised about 80% of the total mass in the universe during this era.

It is not yet certain what exactly dark matter is, but we do know that it does not interact with photons, and only interacts with ordinary matter through the gravitational force, and possibly the weak interaction. Since dark matter is not coupled to photons like ordinary matter is, it did not experience the diffusive smoothing of perturbations, and was able to retain the density fluctuations. Due to this fact, as well as its dominance of the mass

budget in the universe, dark matter was responsible for propagating these perturbations, allowing the difference in densities between different regions of space to amplify over time.

Since dark matter mainly interacts with itself or other matter through gravity, it is a straightforward process to calculate how its density throughout space evolved over time. Starting with the initial density perturbations seen in the CMB and utilizing the physics of frictionless gravitational collapse, cosmologists have run numerical simulations to illustrate how the structure of dark matter would have evolved through the dark ages.

The underdense regions seen in Figure 1.1 become voids containing very little matter; as the universe continues to expand, the voids expand with it. The overdense regions, however, have a high enough density for the matter to become gravitationally bound and therefore exempt from universal expansion. Numerical simulations of dark matter collapse show that overdense regions that become gravitationally bound will contract along all three axes in space: it first flattens into a 2-dimensional sheet ("pancakes"), which then breaks into 1-dimensional filaments. The nodes that lie at the intersections of these filaments are called (dark matter) halos, which are the objects of interest in this project. The structure constituting the cosmic web is illustrated in Figure 1.2.

1.3 Dark Matter Minihalos

According to the standard cold dark matter (CDM) model of cosmology, structure in the universe evolved in a hierarchical fashion, with smaller structures coalescing to form larger

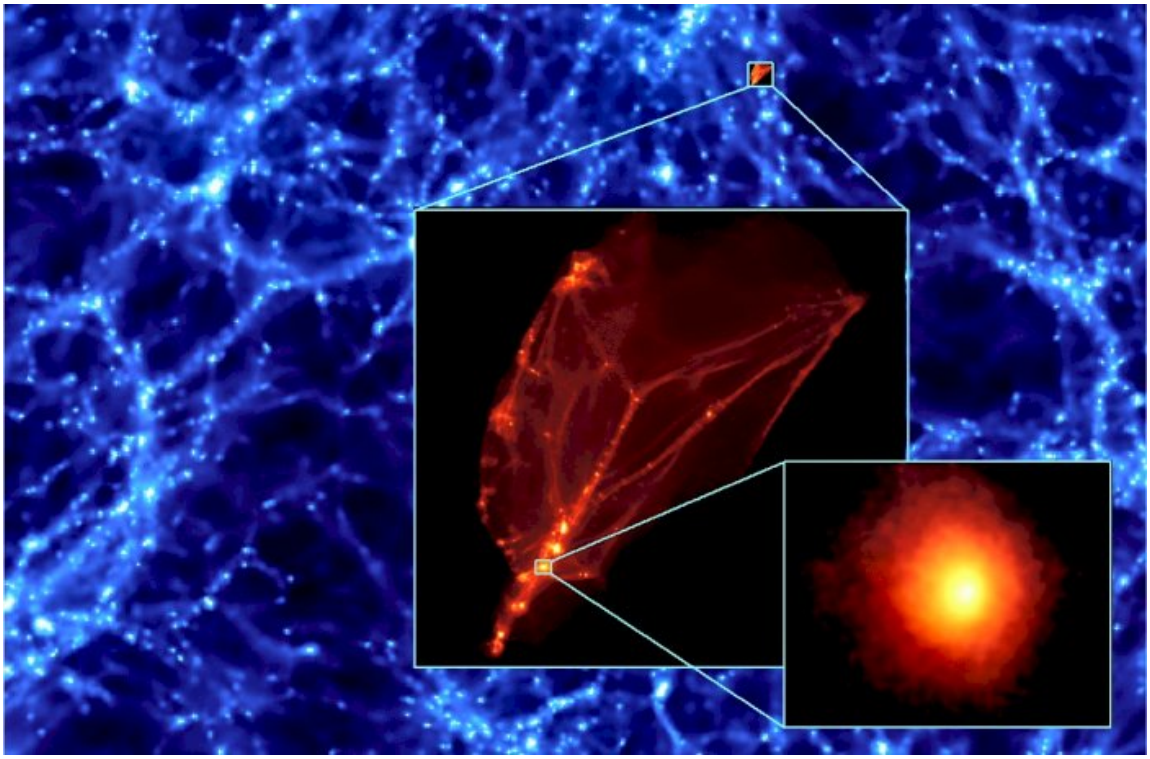

Figure 1.2 As dark matter collapsed in the early universe, it formed a cosmic Web structure. The dark voids continue to expand with the universe, while the denser filaments remain gravitationally bound. In the nodes of these filaments reside dark matter halos. This figure is adopted from Diemand et. al. (2005).

ones. The smaller dark matter halos, termed minihalos, are expected to be the first sites of star formation. They are predicted to comprise $\sim 10^5$ solar masses roughly 100 million years after the Big Bang. Any dark matter halos smaller than this would not have been able to cause the gas to further collapse due to the opposing pressure of thermal motion. Thus, the first stars in the universe must have formed in minihalos with masses of 10^5 or 10^6 solar masses (for reference, the dark matter halo of the Milky Way has a mass of 10^{12} solar masses). These minihalos also had characteristic radii of ~ 100 lightyears, and virial temperatures of $\sim 1000\,\mathrm{K}$ (Bromm et. al. 2009).

For stars to form in minihalos, the gas at the center of minihalos must collapse to sufficiently high densities such that gravity can overwhelm thermal pressure, allowing nuclear fusion to begin. To do so, the gas in minihalos must have a mechanism by which to cool as it collapses. At sufficiently high temperatures, collisions between gas particles will excite the particles into higher energy quantum states; from these unstable states, the particles spontaneously drop back to lower energy states, releasing photons, which carry thermal energy out of the minihalo. In effect, some of the compression heat gained from collapse is released from the minihalo, allowing the gas cloud to collapse further.

However, minihalos only contain primordial gas left over from recombination, which consists of atomic hydrogen, helium, and trace amounts of lithium. Because the energy differences between the lowest quantum states of these atoms are relatively large (compared to molecules and heavier elements), they are only efficient coolants above temperatures of

10^4K. Prior to the creation and distribution of heavy elements by the first stars, gas cooling was reliant on the formation of molecules (particularly, H_2). In this project, my focus is on the formation of molecular coolants, catalyzed by the electrons liberated by an x-ray background. This x-ray background serves as feedback for the first stellar objects that existed in the universe; thus, this project will improve our understanding of how the first stars in the universe influenced the subsequent formation of a new generation of stars.

1.4 Brief Outline

This thesis is structured as follows:

First, the strength of the x-ray background is estimated by characterizing the possible stellar sources that emit x-rays. In particular, we estimate an upper-limit strength for the x-ray background, and then test weaker backgrounds (as we do not have observations that tell us the actual x-ray profile of the early universe).

We already know the contents of minihalos (primordial abundances of elements left over from the Big Bang), as well as the relevant gas physics, so it is straightforward to calculate the heating and ionization rates caused by x-rays on minihalo gas. These rates are then incorporated in a computer simulation that calculates the thermodynamic evolution of a minihalo gas cloud as it collapses in free-fall. The simulation tracks the state of the minihalo, showing how it changes as it collapses under the influence of x-ray backgrounds of varying strengths. In this project, we are most concerned with how temperature and

fragmentation scale evolve during minihalo collapse.

The results from each of the different x-ray backgrounds are compared to the case of no background to see what effect x-rays would have on the evolution of minihalos. Finally, we consider the effect that these differences would have on the stars that form in these minihalos, and how these stars would in turn influence future structure formation in the universe on a larger scale.

Chapter 2

Methods

2.1 X-ray production

To determine the effects of an x-ray background on the thermodynamic evolution of mini-halos, we must first characterize the background by analyzing the possible sources of this background. Three possible x-ray sources are analyzed: high-mass x-ray binaries (HMXBs), core-collapse supernovae (CC SNe), and pair-instability supernovae (PISNe). X-ray binaries consist of a black hole or neutron star and a massive star closely orbiting each other; as matter from the companion star falls onto the black hole, it releases its gravitational energy mostly in the form of x-rays. Core-collapse supernovae (also known as Type II SNe) are the explosions that mark the end of the lives of massive stars ($\sim 8 - 50$ times the mass of the sun); these are caused by a loss of pressure as too much iron and nickel forms in the core, leading to rapid collapse and a violent rebound. Pair-instability supernovae are

expected to occur in stars with masses $\sim 140 - 260$ times the mass of the sun. This type of supernova is more energetic than core-collapse, and is triggered by a loss in thermal pressure at the core when gamma rays are converted into electron-positron pairs (Heger & Woosley 2002).

Energy densities are calculated and compared to determine the relative strength of each source. In deriving expressions for the energy density of the background, we calculate the contribution from Population III stars separately from the contributions from Population I and Population II stars. (Pop III stars are metal-free, while Pop I stars have the highest metallicity; metallicity refers to the fraction of the star's mass that is in the form of elements heavier than hydrogen or helium). We do this to account for the large disparities in stellar mass distribution and formation rates between the two groups.

2.1.1 High Mass X-ray Binaries

The first sources we consider for x-ray production are high-mass x-ray binaries. The energy density of the x-rays produced from HMXBs can be given by the expression

$$u_{\rm XR}(z) \approx l_{\rm Edd}\, t_{\rm life} f_{\rm XRB} \Psi_*(z) t_{\rm H}(z)(1+z)^3 \ . \tag{2.1}$$

The fraction of the mass from the star formation rate Ψ_* that evolves into HMXBs, $f_{\rm XRB}$, is calculated from the fraction of stars forming massive black holes, the fraction of black holes in binary systems, and the fraction of binary systems close enough to in-

duce mass exchange. For Pop III stars, we estimate this efficiency factor to be $f_{\rm XRB} = f_{\rm BH} f_{\rm binary} f_{\rm close} \simeq \left(\frac{1}{2}\right)(1)\left(\frac{1}{5}\right) = 10^{-1}$; for Pop I and Pop II stars, the efficiency factor is estimated to be $f_{\rm XRB} \simeq \left(\frac{1}{100}\right)\left(\frac{1}{2}\right)\left(\frac{1}{5}\right) = 10^{-3}$. The specific Eddington Luminosity, given by $l_{\rm Edd} = 10^{38}\,{\rm erg\,s^{-1}\,M_\odot}^{-1} = L_{\rm Edd}/M_{\rm BH}$, is the maximum luminosity attainable by a stellar object without photon pressure ejecting its gaseous outer layers. For initial calculations, we use an upper limit estimate of the total lifetime of x-ray emission, $t_{\rm life} = 10^7{\rm yr}$. The total x-ray background is accumulated over the Hubble time (which approximates the age of the universe for a given redshift), given by

$$t_{\rm H}(z) \simeq 10^8{\rm yr}\left(\frac{1+z}{20}\right)^{-3/2} \quad . \tag{2.2}$$

These values lead to an expression for $u_{\rm XR}$ as a function of star formation rate and redshift:

$$u_{\rm XR}(z) = \sum_i \alpha_i \left(\frac{\Psi_*(z)_i}{10^{-3}{\rm M_\odot yr^{-1}Mpc^{-3}}}\right) \times \left(\frac{1+z}{20}\right)^{\frac{3}{2}} \tag{2.3}$$

where $u_{\rm XR}$, for HMXBs, is summed over the two species i = Pop III and i = Pop I/II. For Pop III stars, we estimate the normalization factor to be $\alpha \sim 10^{-14}{\rm erg\ cm^{-3}}$, and for Pop I/II stars $\alpha \sim 10^{-16}{\rm erg\ cm^{-3}}$. The star formation rate $\Psi_*(z)$ for each species is taken from figure 1 in Bromm & Loeb (2006).

2.1.2 Supernovae

A similar approach was used to obtain an expression for $u_{\rm XR}$ for core-collapse supernovae (CC SNe) and pair instability supernovae (PISNe):

$$u_{\rm XR}(z) \approx f_{\rm SN} f_{\rm XR} E_{\rm SN} \Psi_*(z) t_{\rm H}(z)(1+z)^3 \ . \tag{2.4}$$

In this equation, $f_{\rm SN} \sim 10^{-2}\,{\rm M}_\odot^{-1}$ is the number of supernovae per mass of star-forming material, $E_{\rm SN}$ is the total shock-wave energy of each supernova, and $f_{\rm XR} \sim 10^{-3}$ is the fraction of $E_{\rm SN}$ channeled into x-rays. Both Pop I/II and Pop III stars that end their lives as core-collapse supernovae are assigned $E_{\rm SN} \sim 10^{51}\,{\rm erg}$, while Pop III stars that end their lives as the more energetic PISNe (Heger et. al. 2003) are assigned $E_{\rm SN} \sim 10^{52}\,{\rm erg}$. The final expression for $u_{\rm XR}$ is identical to that of HMXBs (Eq. 2.4) but with 3 terms: core-collapse SNe for Pop I/II stars ($\alpha \sim 10^{-19}{\rm erg\ cm^{-3}}$), core-collapse SNe for Pop III ($\alpha \sim 10^{-19}{\rm erg\ cm^{-3}}$) and PISNe for Pop III stars ($\alpha \sim 10^{-18}{\rm erg\ cm^{-3}}$). Pop I and II stars do not undergo PISNe since, unlike Pop III stars, their masses do not reach the requisite $140{\rm M}_\odot$. The contributions to the total $u_{\rm XR}$ (2 terms from HXMB's and 3 terms from supernovae) are plotted as a function of redshift in Figure 2.1.

With an x-ray background now established, our next goal is to see the effects this background would have on the thermodynamic evolution of primordial minihalos. As can be seen in Fig. 2.1, the contribution to the x-ray background by SNe is negligible, even in

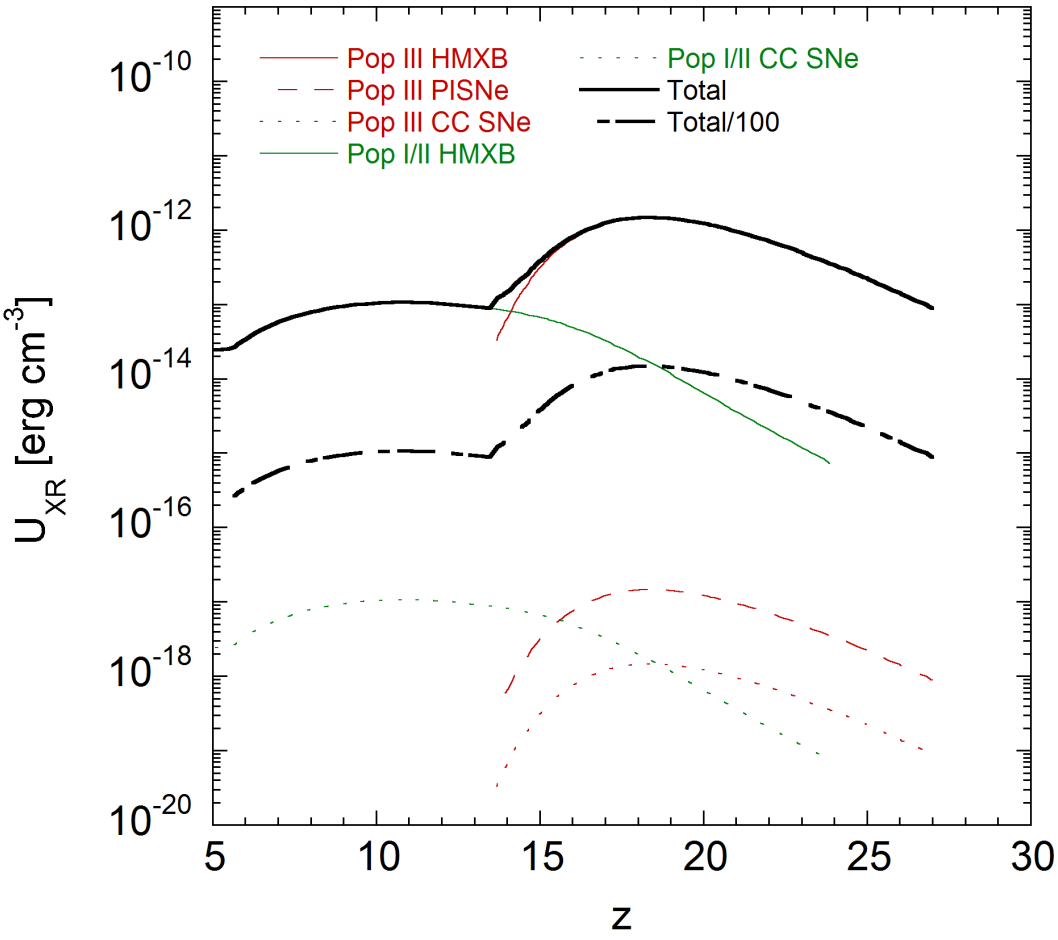

Figure 2.1 Energy density profiles of each source and their aggregate as a function of redshift (i.e. Eq. 2.3). Pop III stars (*red lines*) are the primary contributors to $u_{\rm XR}$ in the early universe, whereas Pop I and II stars (*green lines*) begin to dominate at z $\simeq$ 13.5. Contributions from HMXBs (*solid lines*) are roughly 4 orders of magnitude greater than contributions from core-collapse SNe (*dotted lines*), and PISNe (*dashed lines*) are 10 times greater than CC SNe. Because of the negligibly small contributions from both SNe sources, the total (*black lines*) $u_{\rm XR}$ background is essentially the sum of HMXBs. The total was divided by 100 erg cm^{-3} and plotted (*dashed-dotted line*) to represent a lower-limit estimate of HMXB contribution with $t_{\rm life} = 10^5$yr for Eq. 2.1. The values for Ψ_* were extracted from figure 1 (top graph, dashed lines for Pop III and Pop I/II) of Bromm & Loeb (2006).

the lower-limit case for HMXBs ($t_{\rm life} = 10^5$ yr). For the remainder of this paper, we will only consider x-rays originating from HMXBs. We assume that the x-ray background is isotropic at all redshifts. Statistically, some locations in the universe will begin forming stars at different times and at different rates. Our project looks at regions of space that are forming their Pop III (first generation) stars after Pop III stars in neighboring regions have had the chance to form, die, and emit x-rays.

2.2 Ionization and Heating Rates

The primary photoionization rate, in units of $\rm s^{-1}$, is given by

$$\zeta_{\rm ion} = \int_{\nu_{\rm min}}^{\nu_{\rm max}} \frac{f_\nu \sigma_\nu}{h\nu} d\nu \tag{2.5}$$

where $\nu_{\rm min} = 0.1{\rm keV}/h$ and $\nu_{\rm max} = 10{\rm keV}/h$ are the frequency boundaries within which the non-thermal x-ray radiation dominates.

We assume that the x-ray spectrum is a power-law continuum, $f_\nu = f_0 \left(\frac{\nu}{\nu_0}\right)^\alpha$, where $\alpha = -1$ for x-ray sources. By using the normalization relationship $\frac{c}{4} u_{\rm XR} = \int f_\nu d\nu$, we get an equation for specific flux as a function of energy density and frequency,

$$f_\nu = 6.74 \times 10^{-8} {\rm erg\ cm^{-2}\ s^{-1}\ Hz^{-1}} \left(\frac{u_{\rm XR}}{\rm erg\ cm^{-3}}\right) \left(\frac{\nu}{0.1\,{\rm keV/h}}\right)^{-1} .$$

The photoionization cross sections, σ_ν, for each of the three species (HI, HeI, and HeII)

are obtained from the expressions given in Barkana & Loeb (2001). These values represent probability that a photon hits a target particle. When the integral for ζ is evaluated, we obtain an expression for photoionization rate that is linearly dependent on energy density.

We must also consider the secondary ionizations due to the energetic electrons that were photoionized by x-rays. The secondary ionization rates for HI and HeI are given by

$$\zeta_{\rm sec}[\rm HI] = f_{\rm H}\left(\Gamma_{\rm HI} + \frac{n_{\rm HeI}}{n_{\rm HI}}\Gamma_{\rm HeI}\right)\frac{1}{13.6\,\rm eV} \tag{2.6}$$

$$\zeta_{\rm sec}[\rm HeI] = f_{\rm He}\left(\Gamma_{\rm HeI} + \frac{n_{\rm HI}}{n_{\rm HeI}}\Gamma_{\rm HI}\right)\frac{1}{24.6\rm eV}\ . \tag{2.7}$$

The $\Gamma_{\rm n}$ terms in these two equations are calculated using Eq. 2.11 (Jeon et. al. 2012). We use the analytic fits from Shull & van Steenberg (1985) for the fraction of primary electron energy that goes into secondary ionizations of hydrogen ($f_{\rm H}$) and helium ($f_{\rm He}$), which are

$$f_{\rm H} = 0.3908\left(1 - x_{\rm ion}^{0.4092}\right)^{1.7592} \tag{2.8}$$

$$f_{\rm He} = 0.0554\left(1 - x_{\rm ion}^{0.4614}\right)^{1.6660} \tag{2.9}$$

where $x_{\rm ion} = n_{\rm H+}/n_{\rm H}$ is the hydrogen ionization fraction. We ignore secondary ionizations of HeII as they are negligibly small (Shull & van Steenberg 1985).

The effective ionization rate can therefore be written as

$$\zeta_{\rm eff} = \zeta_{\rm ion}[\rm HI] + \zeta_{\rm ion}[\rm HeI] + \zeta_{\rm ion}[\rm HeII] + \zeta_{\rm sec}[\rm HI] + \zeta_{\rm sec}[\rm HeI] \tag{2.10}$$

Γ is the rate at which excess energy due to the first photoionization of the gas is released; in units of erg cm^{-3} s^{-1}, it is given by

$$\Gamma_{\rm n} = n_{\rm n} \int_{\nu_{\rm min}}^{\nu_{\rm max}} f_\nu \sigma_\nu \left(1 - \frac{\nu_{\rm T}}{\nu}\right) d\nu \ . \tag{2.11}$$

where $n_{\rm n}$ is the number density of the respective species (HI or HeI) and $\nu_{\rm T}$ is the ionization threshold frequency ($h\nu_{\rm T} = 13.6\,{\rm eV}$ for HI, $h\nu_{\rm T} = 24.6\,{\rm eV}$ for HeI, and $h\nu_{\rm T} = 54.4\,{\rm eV}$ for HeII).

The total photo-heating rates of the gas cloud is then given by

$$H = \Gamma_{\rm HI}\left(1 - f_{\rm H}\right) + \Gamma_{\rm HeI}\left(1 - f_{\rm He}\right) + \Gamma_{\rm HeII} \ . \tag{2.12}$$

The $\left(1 - f_{\rm H/He}\right)$ terms take into account the fraction of electron energy lost to secondary ionizations.

The approach taken to obtain heating and ionization rates closely follows the work of Jeon et. al. (2012).

2.3 Dynamic Minihalo Model

To examine the thermodynamic response of primordial gas to the x-ray background, we use the one-zone models from Johnson & Bromm (2006). The code we use to model the evolution of gas clouds is adapted from the version used in Stacy & Bromm (2007).

We first model a minihalo at $z = 25$; at this redshift, the temperature to which the primordial gas can cool is limited to a CMB temperature floor of $T_{\rm CMB} = 2.7{\rm K}\,(1+z) = 70.2{\rm K}$. We use an initial temperature of $T = 200{\rm K}$ so that there is insufficient pressure support to allow the gas to collapse in free-fall (Bromm & Clarke 2002). In free-fall collapse, the density of the gas will evolve as ${\rm d}n/{\rm d}t = n/t_{\rm ff}$. Since the free-fall time is $t_{\rm ff} = (3\pi/32G\rho)^{1/2}$, and the gas density $\rho = \mu m_{\rm H} n \approx m_{\rm H} n$ (the mean molecular weight of primordial gas is $\mu = 1.2$; see Stacy & Bromm 2007), the number density evolves as

$$\frac{{\rm d}n}{{\rm d}t} \simeq \left(\frac{32 G m_{\rm H}}{3\pi}\right)^{1/2} n^{3/2} \; . \tag{2.13}$$

We chose an initial gas density given by the density of baryons in DM halos at the point of virialization (Clarke & Bromm 2003):

$$n_0 \simeq 0.3 \left(\frac{1+z}{20}\right)^3 {\rm cm}^{-3} \; . \tag{2.14}$$

Primordial abundances are assumed for all chemical species (hydrogen, helium, deuterium, and free electrons), given in Bromm et. al. (2002).

The effects of the x-ray background on minihalos are taken into account with the insertion of the ionization (Eq. 2.10) and heating (Eq. 2.12) rates into the code. For different background strengths, the heating and ionization terms are recalculated using different values for $u_{\rm XR}$, as given by the totals in Fig. 2.1 at a given redshift (here $z = 25$).

Chapter 3

Results

3.1 Thermal and chemical evolution

The comprehensive chemical reaction network is solved using all the chemical species included in Johnson & Bromm (2006). These chemical species (H, H^+, H^-, H_2, $H_2{}^+$, e^-, He, He^+, He^{++}, D, D^+, HD, D^-, and HD^+) are entered into a network of 18 reactions. Using this model, we compute the thermal and chemical evolution of the primordial clouds via programming in C. The code we use is adapted from Stacy & Bromm (2007). In particular, we calculate the abundance of free electrons, H_2, and HD as a function of the hydrogen number density $n_{\rm H}$ (Fig. 3.1), the temperature (Fig. 3.2), and the fragmentation scale (Fig. 3.3).

For each parameter, we consider 4 different strengths of the x-ray background: our upper-limit estimate of $u_{\rm XR}$ given by the total in Fig. 2.1 (which we will refer to as the

"Maximum" background), this maximum $u_{\rm XR}$ divided by 100, the maximum $u_{\rm XR}$ divided by 10^5, and the case of no x-ray background ($u_{\rm XR} = 0$).

The lowest temperature to which the primordial gas can cool is limited by the CMB temperature (the CMB floor). In the no-background case, the temperature to which the gas can cool is impeded as the primordial gas collapses past $n_{\rm H} \sim 10^4\,{\rm cm}^{-3}$, after which the gas starts to heat up again; in our three background cases, the temperature can continue to decrease at high densities. The precipitous drops seen in the temperature graph (for the three non-zero backgrounds) occur at the same densities as the jumps in H_2 and HD abundance as well as the drops in the electron abundance.

We focus on the $u_{\rm XR} = {\rm Max}/10^5$ case to illustrate the situation where we find the lowest temperatures. We found that background strengths ranging from $u_{\rm XR} = {\rm Max}/10^2$ to $u_{\rm XR} = {\rm Max}/10^8$ are needed to cool minihalo gas below the no-background case. Furthermore, the temperature can reach the CMB floor for $u_{\rm XR} = {\rm Max}/10^3$ to $u_{\rm XR} = {\rm Max}/10^6$.

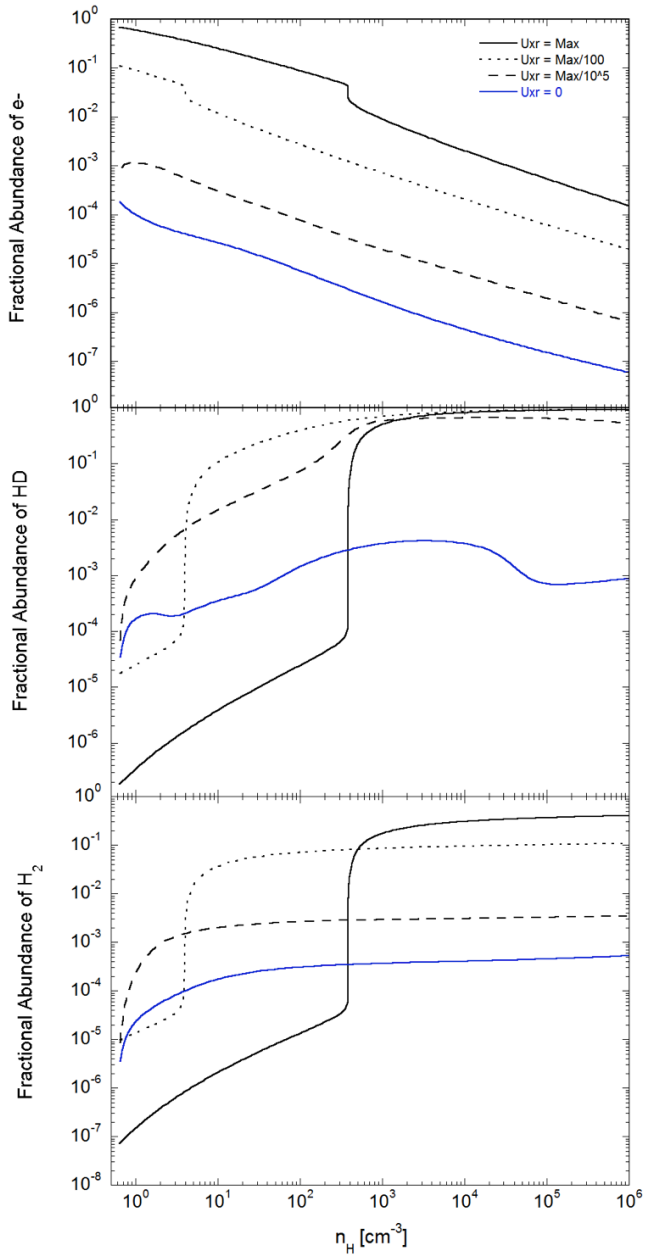

Figure 3.1 Simulation results for the fractional abundances of three chemical species as a function of hydrogen number density $n_{\rm H}$ at redshift $z = 25$. The three graphs show the fractional abundance of free electrons to all hydrogen species (*top*), fractional abundance of HD to all deuterium species (*middle*), and fractional abundance of H_2 to all hydrogen species (*bottom*) For each graph there are 4 scenarios to demonstrate the effects of different strengths of the x-ray background. In the plot labels, $u_{\rm XR}$ = Max refers to the upper-limit estimate. The dashed-dotted lines assume that $u_{\rm XR}$ is at its estimated upper-limit (i.e. the black solid line in Fig. 2.1) with $\alpha \sim 10^{-14}$ in Eq. 2.3. For the dotted lines and dashed lines, the maximum $u_{\rm XR}$ is divided by 10^2 and 10^5 ($\alpha \sim 10^{-16}$ and $\alpha \sim 10^{-19}$), respectively. The solid line corresponds to a non-existent x-ray background.

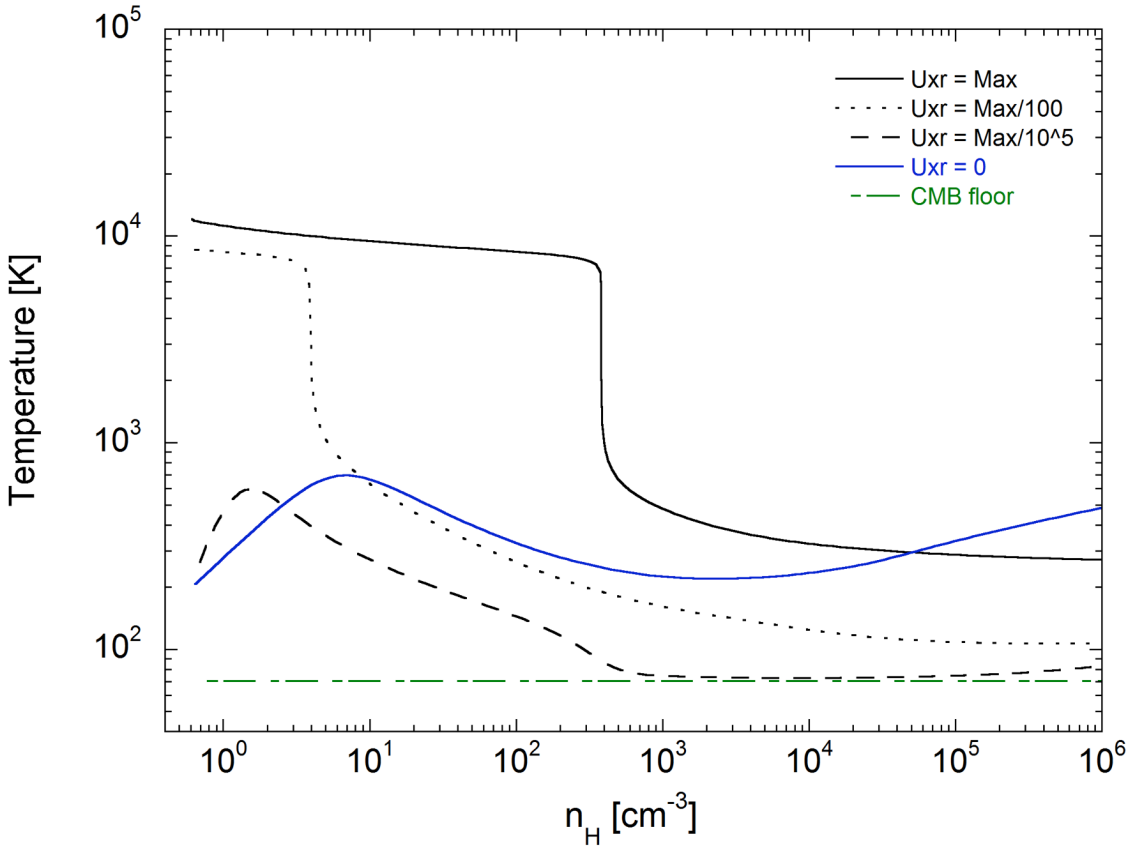

Figure 3.2 Simulation results for the evolution of the temperature of a minihalo as it collapses. The x-ray backgrounds (the four curves) are the same as in Fig. 3.1. In this graph, a green dashed line is added to represent the CMB floor of $T = 70.2$K at redshift z = 25, which is the minimum possible temperature that a minihalo can reach. The precipitous drops in temperature seen in the two most energetic backgrounds occur at the same densities as the spikes in H_2 and HD abundances, confirming that minihalo cooling is a direct result of the formation of these molecules.

3.2 Fragmentation scale

The decrease in the minimum temperature a minihalo can reach due to x-rays implies that the fragmentation scale of the gas clouds would also be lowered. We calculate the new fragmentation scales with the Bonnor-Ebert mass, given by (e.g. Johnson & Bromm 2006)

$$M_{\rm BE} \simeq 700\,{\rm M}_{\odot} \left(\frac{T_{\rm f}}{200\,{\rm K}}\right)^{3/2} \left(\frac{n_{\rm f}}{10^4\,{\rm cm}^{-3}}\right)^{-1/2} , \tag{3.1}$$

where n_f and T_f are the density and temperature of the gas at which the fragmentation occurs. We use this equation to calculate the Bonnor-Ebert mass for a cloud collapsing in free fall, corresponding to the temperature graph in Fig. 3.2; we show the results in Fig. 3.3 for the same 4 cases as in Section 4.1: the maximum $u_{\rm XR}$, the maximum $u_{\rm XR}$ divided by 100, the maximum $u_{\rm XR}$ divided by 10^5, and the no background case ($u_{\rm XR} = 0$).

Our results for the Bonnor-Ebert mass reflect the results for temperature evolution; the lowest fragmentation scale is attained with a background strength of $u_{\rm XR} = {\rm Max}/10^5$. Also, background strengths ranging from $u_{\rm XR} = {\rm Max}/10^2$ to $u_{\rm XR} = {\rm Max}/10^8$ are needed for the fragmentation scale to be below the no-background case.

According to Mackey et al. (2003), we can assume that the Bonnor-Ebert mass gives a reasonable approximation for the characteristic masses of Population II.5 stars. Pop II.5 stars are metal-free but have lower masses than Pop III stars due to molecular cooling. The efficiency with which this mass is converted into stars is unknown for the high redshift universe (Johnson & Bromm 2006), so the Bonnor-Ebert mass gives an upper-limit on the masses of Pop II.5 stars.

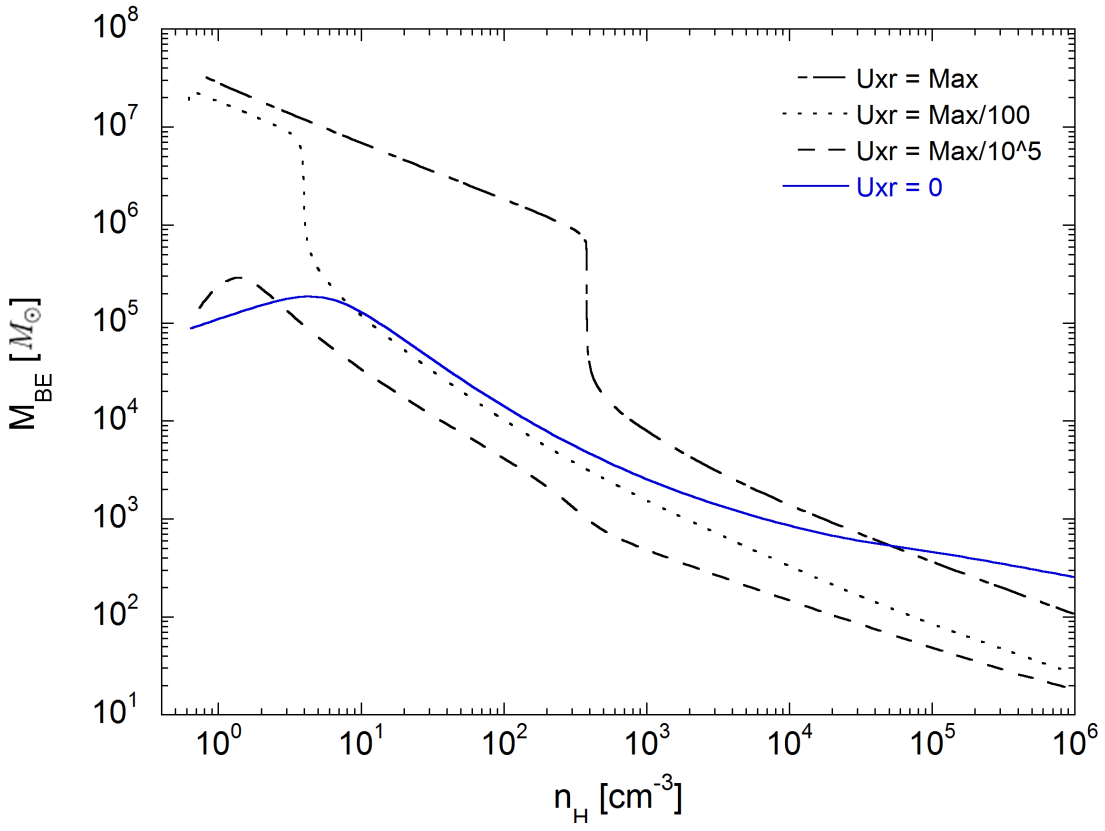

Figure 3.3 Bonnor-Ebert Mass as a function of hydrogen number density for free-falling gas clouds inside minihalos at redshift $z = 25$. This depicts the mass scale at which gas could potentially fragment at each stage in minihalo collapse. Above $n_{\rm H} \sim 10^5$ cm^{-3}, the Bonnor-Ebert mass is equivalent to the characteristic mass of a star that could form in the center of the minihalo.

3.3 Heating/Cooling Timescale

To test the validity of the temperature results, we calculate and compare the characteristic timescales for heating and cooling for the 4 backgrounds considered.

The heating timescale is given by

$$t_{heat} = \frac{n\, k_B\, T}{\Gamma_{\rm heat}} \ , \tag{3.2}$$

where n is the total gas number density, T is the temperature, and $\Gamma_{\rm heat}$ the rate at which the energy of the minihalo increases, given by $\Gamma_{\rm heat} = \Gamma_{\rm AD} + H$. The x-ray heating rate H is given in Eq. 2.12, and $\Gamma_{\rm AD}$ is the adiabatic heating term given by

$$\Gamma_{\rm AD} = \frac{n\, k_B\, T}{t_{\rm ff}} \ . \tag{3.3}$$

The cooling timescale $t_{\rm cool}$ is given by an expression similar to Eq. 3.2, but with $\Gamma_{\rm heat}$ replaced by $\Lambda_{\rm cool}$, which is the rate at which energy escapes the minihalo. $\Lambda_{\rm cool}$ results from H_2 and HD transitions, and atomic line cooling (collisional ionization, recombination, collisional excitation, and Compton cooling). When the cooling timescale is shorter than the heating timescale, the gas experiences a net cooling.

Figure 3.4 shows the calculated timescale ratios for the 4 background cases.

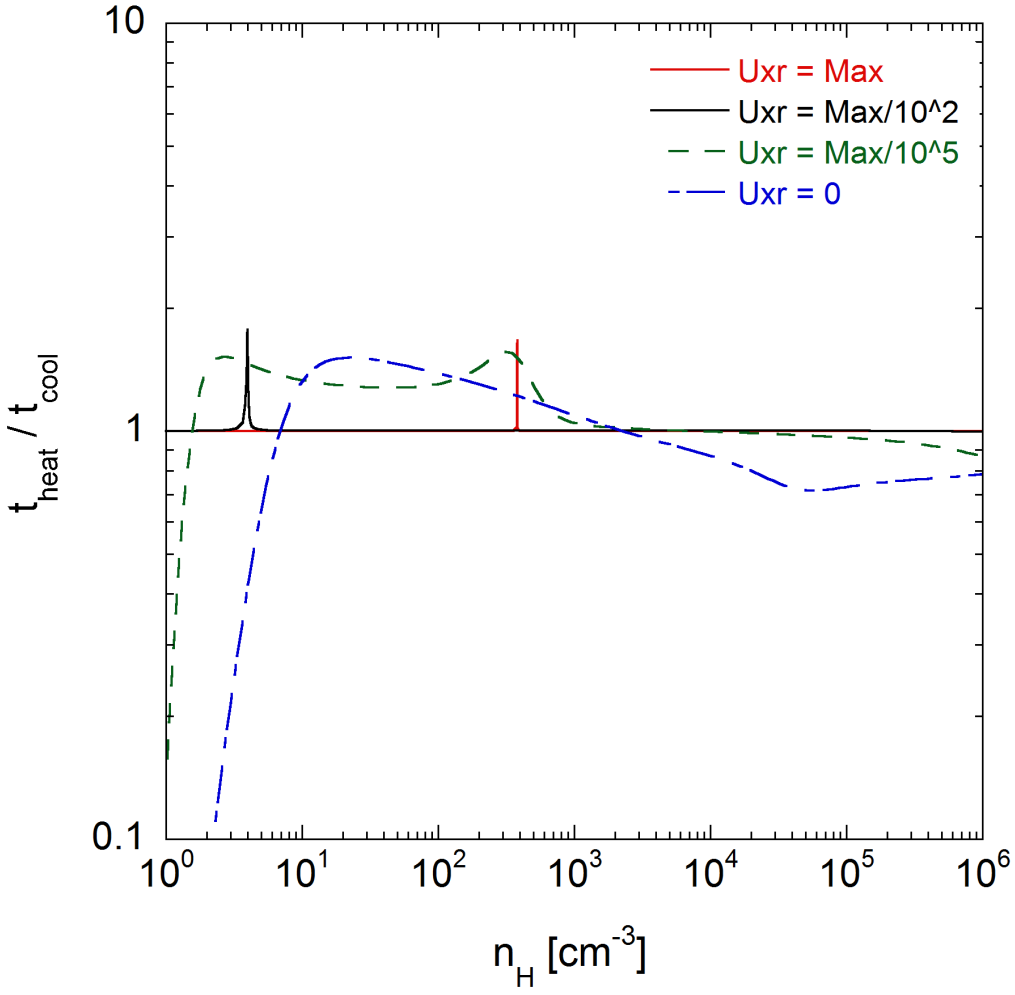

Figure 3.4 Ratio of the heating timescale to the cooling timescale of a minihalo at $z = 25$ as a function of hydrogen number density. Lines above the $t_{\rm heat}/t_{\rm cool} = 1$ line have a longer heating timescale than cooling timescale, and so indicate net cooling. The solid red curve shows the maximum $u_{\rm XR}$, which has roughly equal heating and cooling timescales until the peak, which occurs at the same density as the precipitous temperature drop seen in Figure 3.2; the same is true for the maximum/100 case.

Chapter 4

Conclusion

Overall, we found that a sufficiently energetic x-ray background in the early universe would provide negative feedback (net heating) to minihalos; as the x-ray energy is reduced, the background instead provides positive feedback (net cooling) to the minihalo gas, and could allow the gas to reach the lowest possible temperature set by the Cosmic Background Radiation (~ 70 K at $z = 25$) for sufficiently weak backgrounds.

The upper-limit estimate of the energy density of an x-ray background at $z = 25$, $u_{\mathrm{XR}} = 10^{-14}\mathrm{J/m}^3$, caused a precipitous drop in temperature once the simulated minihalo collapsed to a density of $n_{\mathrm{H}} \sim 4\times10^{-4}\mathrm{m}^{-3}$, likely caused by the spike in H_2 abundance seen in Figure 3.1. However, the temperature remained above the no-background case until the minihalo gas reached a density of $n_{\mathrm{H}} \sim 10^{-4}\,\mathrm{m}^{-3}$. Minihalo conditions are pertinent when the gas surpasses this density since this is when star formation begins. In this project, we were ultimately concerned with how alterations in a minihalo's conditions affect the characteristics of the stars that form inside them. In all test cases for x-ray backgrounds of varying energy density, including the upper-limit estimate, the temperature and Bonnor-Ebert mass (the characteristic mass of new stars forming at the center of minihalos) were

reduced to below the no-background case.

As the x-ray energy density was reduced below our established upper-limit, both temperature and fragmentation scale (Bonnor-Ebert mass) decreased, which suggests the formation of less massive stars. In the range of energy densities from $u_{\mathrm{XR}} = 10^{-20}\mathrm{J/m^3}$ to $u_{\mathrm{XR}} = 10^{-17}\mathrm{J/m^3}$, minihalo gas was able to cool to the CMB floor. This is indicative of cooling by HD, since H_2 is only capable of reducing gas temperature to a few hundred Kelvin. The energy density at which maximum cooling (lowest temperatures and fragmentation scales) was obtained is $u_{\mathrm{XR}} = 10^{-19}\mathrm{J/m^3}$. When the energy density was set to below $u_{\mathrm{XR}} = 10^{-22}\mathrm{J/m^3}$, the effects of x-rays became negligible, and temperature and fragmentation scale converged to the no-background case.

To summarize, most x-ray backgrounds that we tested were able to provide positive thermal feedback in minihalo gas, which in turn would cause less massive stars to form in the center of these minihalos. This would have been vital to future structure formation since the mass of stars influence the abundance of metals they produce and disperse in the surrounding media through fusion and supernovae (in astronomy, metals refer to any elements other than hydrogen and helium). The "metallicity", or fractional abundance of heavy elements, of the early universe would affect the thermal evolution of surrounding gas, which would in turn alter the characteristics of future structure formation (i.e. galaxies). If the stars were massive enough, they may have ended their lives through Pair-Instability Supernovae, which are highly luminous (and thus more easily observed than core-collapse supernovae) but would have left no remnants (i.e. black holes or neutron stars). In contrast, stars with sufficiently low mass may have survived to the present, and could be observed in our local neighborhood.

The work done in this project was theoretical. A variety of energy densities were used for x-ray backgrounds partly because our estimates were very idealized, due to the

limited information available on the Dark Ages of the universe. Fortunately, there are several next-generation telescopes being built that will illuminate the conditions during this era. The James Webb Space Telescope (JWST), the successor to the Hubble Space Telescope, will be used to image the very faint, first galaxies of the Universe, and possibly detect metal-free Population III stars, which have yet to be seen. Also in construction are several very large ground-based telescopes with apertures ranging from 24 to 42 meters, including the European Extremely Large Telescope, the Giant Magellan Telescope, and the Thirty Meter Telescope. Ground based telescopes will be used to survey large samples of early galaxies and map the distributions of hydrogen (Loeb 2010). We anticipate that the new observations provided by these future telescopes will impose stricter constraints on conditions in the early universe, allowing us to test our theoretical predictions.

Bibliography

[1] Barkana R., Loeb A., 2001, Phys. Rep., 349, 125

[2] Bromm V., Clarke C. J., 2002, ApJ, 566, L1

[3] Bromm V., Coppi P.S., Larson R. B., 2002, ApJ, 564, 23

[4] Bromm V., Loeb A., 2006, ApJ, 642, 382

[5] Bromm V., Yoshida N., Hernquist L., & McKee C.F., 2009, Nature, 459, 49-54

[6] Clarke C. J., Bromm V., 2003, MNRAS, 343, 1224

[7] Diemand, J. et. al., 2005, Nature, 433, 389-391

[8] Haiman Z., Rees M. J., & Loeb A., 1996, ApJ, 476, 458

[9] Heger A., Fryer C.L., Woolsey S.E., Langer N., & Hartmann D.H., 2003, ApJ, 591, 288

[10] Heger A., Woolsey S.E., 2002, ApJ, 567, 532

[11] Jeon M., Pawlik A. H., Greif T. H., Glover S.C.O., Bromm V., Milosavljevic M., & Klessen R. S., 2012, ApJ, 754, 34

[12] Johnson J. L., Bromm V., 2006, MNRAS, 366, 247

[13] Loeb A., 2010, *How Did the First Stars and Galaxies Form?*, Princeton University Press, Princeton, NJ

[14] Mackey J., Bromm V., Hernquist L., 2003, ApJ, 586, 1

[15] Stacy A., Bromm V., 2007, MNRAS, 382, 229